



## OPEN An upper-limb teleoperation exoskeleton with stepless arm-length parameterization and adaptive force-triggered impedance blending

Puyi Zeng<sup>1,3</sup>, Yuqin Xu<sup>1</sup>, Shaobin Zheng<sup>1</sup>, Shisheng Zhang<sup>2,3</sup>, Chi Zhu<sup>1</sup>, Ruisen Huang<sup>1</sup> & Yang Zhang<sup>1</sup>✉

Remote control technology is a core means of ensuring personnel safety in high-risk scenarios such as deep-sea exploration and nuclear facility maintenance. However, existing exoskeleton teleoperations suffer from drawbacks such as discretized arm length adjustment, insufficient dynamic control adaptability, and limited execution accuracy. This study proposes a reproducible unilateral upper limb exoskeleton teleoperation system, employing a 7-DOF active drive architecture (3 DOF for the shoulder, 1 DOF for the elbow, and 3 DOF for the wrist) to match the kinematic characteristics of the human upper limb. The system integrates four key designs: low-inertia, high-reaction joints (weight reduction using carbon fiber and aluminum alloy), an ergonomic alignment mechanism adapted to upper arm circumferences of 74.8–105.7 mm, a 6-DOF passive compensation module for scapulothoracic wall motion, and a digital adaptive arm length adjustment mechanism (achieving stepless adjustment and dynamic updating of the URDF model through a sliding rheostat). The control strategy adopts a hybrid scheme of “master-end position impedance control and slave-end force-based impedance feedback,” modeled based on the Lagrange equation, introducing adaptive weighted coefficient balance trajectory tracking and force feedback compliance, and verifying global asymptotic stability using Lyapunov functions and the LaSalle invariance principle. The experiment used the Franka Panda robot as a platform, based on a Linux real-time kernel and ROS architecture, with joint position data transmitted via 500 Hz Ethernet. Master-slave teleoperation achieved a mirrored reproduction of a spatial figure-eight trajectory, and gravity compensation effectively offset the load. Ablation experiments showed that the peak contact force in group C3 decreased to 7.41 N (a 68.8% reduction from baseline); the sum of squared residuals in arm length measurement was  $< 0.002 \text{ mm}^2$ , and the deviation after multiple wearing cycles was  $\leq 2.5 \text{ mm}$ . The experiment confirmed that the system overcomes the adaptability and robustness deficiencies of traditional systems, achieving high-precision master-slave synchronization and load compensation. It meets the teleoperation needs of high-risk scenarios and can also provide a rehabilitation training platform for hemiplegic patients, demonstrating broad application prospects.

**Keywords** Upper-limb teleoperation exoskeleton, Stepless arm-length parameterization, Adaptive force-triggered impedance blending

In high-risk operational scenarios such as deep-sea exploration, disaster response, counterterrorism operations, space exploration, and nuclear facility operation and maintenance, direct human involvement poses significant health and life risks due to physiological constraints. Furthermore, in areas with limited medical resources, delays in emergency surgery often exacerbate health crises<sup>1</sup>. In the 21st century, robotics technology has made

<sup>1</sup>Sino-German College of Intelligent Manufacturing, Shenzhen Technology University, Shenzhen, China. <sup>2</sup>Shenzhen Institutes of Advanced Technology, Chinese Academy of Sciences, Shenzhen, China. <sup>3</sup>Puyi Zeng and Shisheng Zhang contributed equally to this work. ✉email: zhangyang@sztu.edu.cn

significant progress. Underwater robots<sup>2</sup>, rescue robots<sup>3</sup>, space operation robots<sup>4</sup>, and nuclear emergency robots<sup>5</sup> have been gradually applied to these fields. However, existing systems have significant limitations in terms of intelligence: they primarily rely on repetitive tasks within structured environments. Deep learning-based systems, while performing well in specific tasks, lack adaptability to unforeseen environmental changes<sup>6</sup>. Furthermore, the lack of understanding of human behavioral patterns further amplifies the uncertainty of human-robot collaboration<sup>7</sup>. Therefore, “human-robot collaborative” teleoperation technology, which combines the advantages of human high-level decision-making with the precise operation capabilities of robots, has become an inevitable trend in the development of high-risk operations<sup>8</sup>.

Teleoperation represents a critical technological paradigm that empowers human operators to accomplish targeted tasks through remote manipulation of robotic systems<sup>9</sup>. This approach has been extensively deployed across multifaceted application domains, including deep-sea operations<sup>10</sup>, space exploration<sup>11</sup>, disaster search and rescue, nuclear waste disposal<sup>12</sup>, mine and explosive clearance, remote surgical procedures<sup>13</sup>, and rehabilitation training<sup>14,15</sup>.

The 1940s marked the Argonne National Laboratory’s pioneering development of model M1, the inaugural master-slave teleoperation system designed for handling highly radioactive nuclear substances, thereby establishing the foundational framework for teleoperation technology<sup>8</sup>. In 2011, NASA deployed the teleoperated Robonaut robot to the International Space Station aboard the discovery spacecraft, enabling execution of complex internal and external station operations<sup>16</sup>. The medical domain has been significantly advanced by Intuitive Surgical’s da Vinci Surgical System (2000), which has evolved into the predominant surgical platform, enhancing procedural accuracy through minimally invasive techniques while enabling remote surgical interventions and reducing recurrence risks<sup>17</sup>. Additionally, the Applied Physics Laboratory’s master-slave teleoperated robotic arm system is specifically engineered for high-radiation nuclear power plant maintenance and decommissioning, facilitating safe high-risk operations via seamless human-robot collaboration<sup>12</sup>.

Teleoperation devices are classified into two distinct categories (Table 1): non-contact and contact-based systems. Non-contact modalities (e.g., optical sensing, eye tracking, inertial measurement units) rely on sensor-mediated interaction but exhibit inherent limitations, including data drift, line-of-sight constraints, and inability to deliver precise force feedback. Most systems restrict operations to end-effector-centric tasks, with compromised attitude control and high-precision dexterous manipulation capabilities, thereby diminishing user immersion<sup>18,19</sup>. Contact-based interfaces (including EEG caps, master manipulators, data gloves, and exoskeletons), physically interfaced with the operator, enable accurate kinematic acquisition and enhanced force interaction. While master manipulators support basic force feedback, they remain constrained to end-effector operations; exoskeletons uniquely provide integrated posture control and force feedback fidelity, rendering them optimal for humanoid robot teleoperation.

This paper is organized as follows: section “**Related work**” explores various exoskeleton systems for teleoperation, outlining their advantages and disadvantages and describing desired exoskeleton characteristics. Section “**Control strategy**” focuses on the system description of the teleoperation exoskeleton, including design requirements, kinematic architecture, and key mechanical design and performance indicators. Section “**Experiment**” discusses the master-slave mapping relationship and control strategy. Section verifies the feasibility of the teleoperation system through experiments. Finally, Section “**Conclusion**” summarizes the research conclusions of this paper.

## Related work

In recent years, significant advancements have been made in upper-limb exoskeleton teleoperation and rehabilitation technologies, with research primarily focusing on two core control strategies: Joint Motion Control and Flexible Interactive Control (Table 2). For teleoperation scenarios, representative studies include Yasuhiro Ishiguro et al. (2020), who proposed a whole-body exoskeleton cockpit based on Flexible Interactive Control to achieve humanoid robot motion coordination<sup>20</sup>; Joao Ramos et al. (2020) applied the same control strategy to lower-limb teleoperation systems, emphasizing bidirectional feedback-driven dynamic synchronization<sup>21</sup>; Marcello Palagi et al. (2024) adopted Joint Motion Control for upper-limb teleoperation, focusing on precise joint trajectory mapping<sup>22</sup>; while N. Hayami et al. (2024) and Alexander Toedtheide et al. (2023) further optimized Flexible Interactive Control for teleoperation, enhancing human-robot interaction transparency<sup>23,24</sup>. For rehabilitation applications, Amin Zeiaee (2022), Pan et al. (2023), and Zheng et al. (2024) developed upper-limb exoskeletons based on Flexible Interactive Control or Joint Motion Control, focusing on motion assistance

Research status	Site of action	Site of action	Wearable	Mechanical structure
Wearable exoskeleton	Human upper limb	✓	✓	✓
Series and parallel force feedback master hand	Human hand	✓	×	✓
Virtual reality data gloves	Human hand	×	✓	×
Force feedback data gloves	Human hand	✓	✓	✓

**Table 1.** Research on the human-computer interaction equipment of the teleoperation host.

Author, (Year)	Wearing part	Application scenarios	Control strategy
Joao Ramos et al. (2018) <sup>21</sup>	Lower limbs	Teleoperation	Flexible interactive control
Yasuhiro Ishiguro et al. (2020) <sup>20</sup>	Upper limbs	Teleoperation	Flexible interactive control
Amin Zeiaee (2022) <sup>25</sup>	Upper limbs	Rehabilitation	Flexible interactive control
Liu et al. (2022) <sup>38</sup>	Lower limbs	Rehabilitation	Joint motion control
Ning et al. (2023) <sup>27</sup>	Upper limbs	Rehabilitation	Joint motion control
Pan et al. (2023) <sup>26</sup>	Upper limbs	Rehabilitation	Flexible interactive control
Alexander Toedtheide et al. (2023) <sup>23</sup>	Upper limbs	Teleoperation	Flexible interactive control
Zhang et al. (2024) <sup>39</sup>	Lower limbs	Rehabilitation	Joint motion control
Marcello Palagi et al. (2024) <sup>22</sup>	Upper limbs	Teleoperation	Joint motion control
Alejandro Suarez et al. (2024) <sup>24</sup>	Upper limbs	Teleoperation	Flexible interactive control
Zheng et al. (2024) <sup>40</sup>	Upper limbs	Rehabilitation	Joint motion control
N. Hayami et al. (2024) <sup>41</sup>	Upper limbs	Teleoperation	Flexible interactive control

**Table 2.** Classification of upper limb exoskeletons.

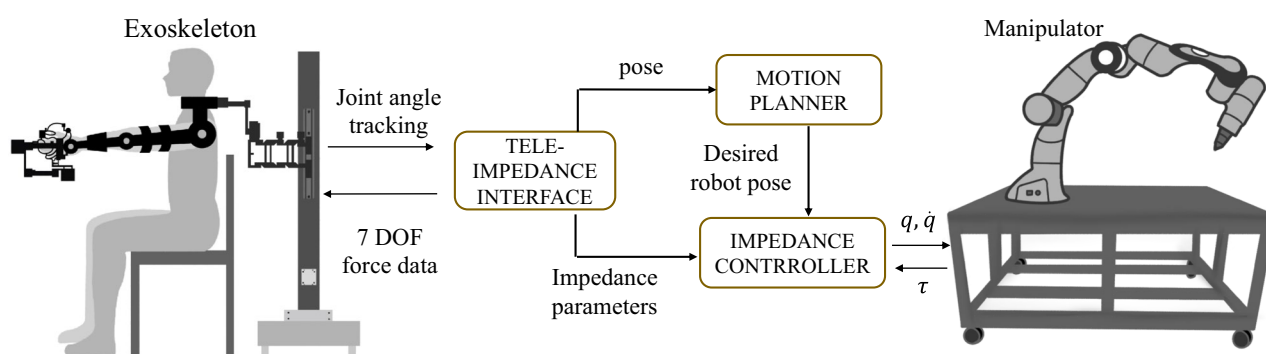


**Fig. 1.** Upper limb exoskeleton teleoperation mode.

and functional recovery<sup>25–27</sup>. These studies have laid a foundation for exoskeleton system development through innovations in control architecture and human-robot interaction mechanisms.

Despite these progresses, existing exoskeleton teleoperation systems still face three key limitations closely related to current control and application characteristics: (1) Existing exoskeleton systems mostly employ discrete mechanical adjustment mechanisms, allowing switching between a few preset arm lengths, making it difficult to accurately match the actual forearm lengths of different users. Furthermore, traditional arm length adjustment methods typically only adjust the mechanical structure, making it impossible to visualize and update the geometric parameters of the model in real time. This necessitates manual offline modification of model parameters before or after use, a cumbersome process prone to introducing errors. (2) Limited adaptability of dynamic control: Joint Motion Control-based systems<sup>22</sup> focus on trajectory tracking but lack robustness in complex dynamic scenarios, while Flexible Interactive Control solutions<sup>20,21</sup> often neglect whole-body coordination (e.g., arm-trunk synergy), reducing balance maintenance capabilities during dynamic operations. (3) Inadequate execution precision: Both control strategies predominantly rely on position/torque-level joint control, lacking low-latency and high-precision torque control mechanisms, which hinders the execution of complex tasks.

Therefore, this study employs a repeatable upper limb exoskeleton engineering approach. The proposed scheme achieves stepless continuous adjustment within the allowable arm length range. Real-time arm length is acquired via a sliding rheostat, parameterized and mapped onto the exoskeleton's geometric model, and relevant joint spacing and kinematic parameters are dynamically updated online. This ensures precise adaptation to different individuals' arm lengths while enabling automatic synchronous adjustment of model parameters, providing a foundation for individualized modeling and accurate master-slave mapping. Simultaneously, through exoskeleton dynamics modeling and dynamic stability control strategies, the system significantly improves operational accuracy and real-time adaptability in complex scenarios, as shown in Figure 1.

## Mechanical design and kinematics

### Requirements of design

Based on anthropometry/biomechanics data<sup>15,28,29</sup> and medical/electrical equipment standards (UNE-EN ISO 12100, UNE-EN ISO 14971, UNE-EN 60204-1), functional and safety requirements are clearly defined, and quantitative constraints are prioritized to ensure academic rigor: (1) Kinematic compatibility: Adapt to the anatomical differences of the target population to ensure consistency with the natural joint movements of the

human upper limb; (2) Torque safety: The joint output torque is limited to  $\leq 80\%$  of the maximum physiological value of the human body to avoid tissue damage<sup>30,31</sup>; (3) Movement stability: Maximum angular velocity  $\leq 120^\circ/\text{s}$  (linear equivalent 200 mm/s), acceleration  $\leq 3.6 \text{ rad/s}^2$ ; (4) Safety mechanism: Equipped with an emergency stop button and a jamming detector to achieve real-time risk mitigation.

### Kinematic architecture

The AIMech exoskeleton employs a 7-DOF active actuation architecture (3 DOFs in the shoulder, 1 DOF in the elbow, and 3 DOFs in the wrist) to match the kinematic characteristics of the human upper limb<sup>32</sup>, as shown in Fig. 2. Based on the 50th percentile male upper limb dynamics model<sup>33</sup>, the human joint movement patterns were confirmed using the 3Dbody platforms (Fig. 3).

### Key mechanical design and performance indicators

Following the integrated electromechanical system design methodology<sup>34</sup>, the system prioritizes performance indicators such as reverse drive capability, low inertia, axis alignment accuracy, and force sensing accuracy, achieving these goals through structural design optimization:

1. Low inertia and high counteracting actuation joint design: All active joints utilize low reduction ratio modules (shoulder: RobStride Dynamics RS 03; elbow/wrist: DAMIAO DM4340/DM4310) to enhance counteracting actuation—crucial for teleoperation transparency and human motion tracking. Structural components are constructed from carbon fiber and aluminum alloy to minimize inertia, reduce drag, and improve dynamic responsiveness. The overall system weight is optimized for gravity-compensated operation, eliminating the user's load burden during remote control missions.
2. Anthropometric Adaptation: To ensure kinematic compatibility among different individuals, the adaptive alignment system integrates the following functions: the symmetrical gear coupling fixing mechanism<sup>35</sup> and the forearm sliding mechanism enable automatic centering of the upper arm (upper arm circumference range: 74.8–105.7 mm) and free rotation of the forearm without affecting the transmission stiffness (Fig. 4). These design features achieve the adaptability of the exoskeleton to the human body and minimize motion interference.
3. Scapulothoracic Wall Motion Compensation: A 6-DOF passive compensation module<sup>26</sup> addresses scapular motion incompatibility and reduces physical interface stress (Fig. 5): 1 translational degree of freedom (linear guide with displacement encoder) compensates for acromion elevation, using constant force springs and steel cables for gravity balance; 3 rotational degrees of freedom (dual-plane linkage mechanism) decouple sagittal/horizontal plane motion, equipped with mechanical locking and incremental encoders for position tracking; ball joint drive (an additional 2 degrees of freedom) enables dynamic coupling between the exoskeleton and the trunk, adapting to complex scapulothoracic wall movements.
4. To address the shortcomings of existing exoskeleton arm length adjustment schemes, such as discrete settings that cannot adapt to continuous anatomical differences in user upper limb length, a lack of real-time parameter visualization, and the need for offline manual model modification, this study proposes a digital adaptive arm length adjustment mechanism (Fig. 6). By integrating a sliding rheostat at the upper and lower arm rails, the continuous mechanical changes in arm length are converted into measurable electrical signals, achieving stepless adjustment within the physiological arm length range. The core implementation process

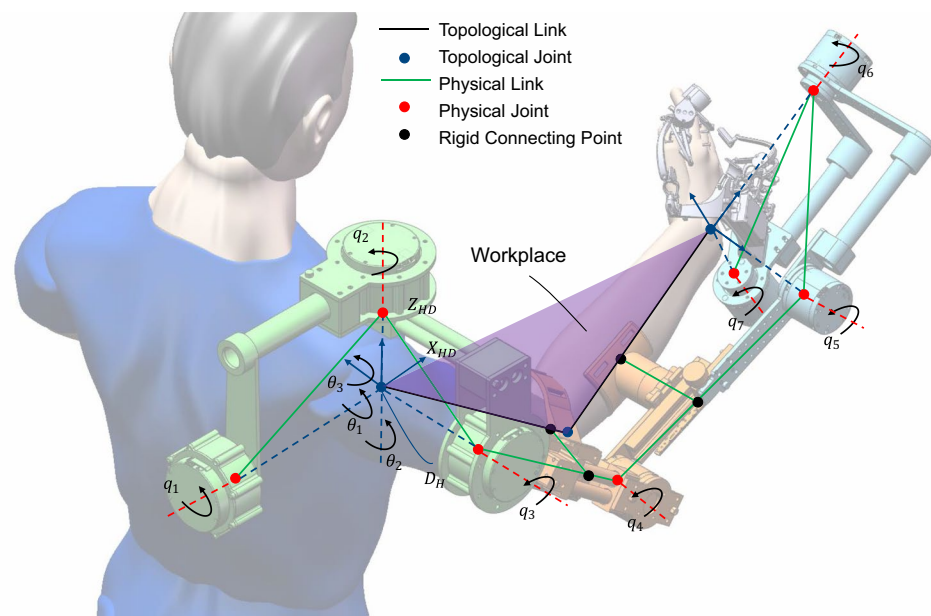


**Fig. 2.** AIMech exoskeleton CAD structure.

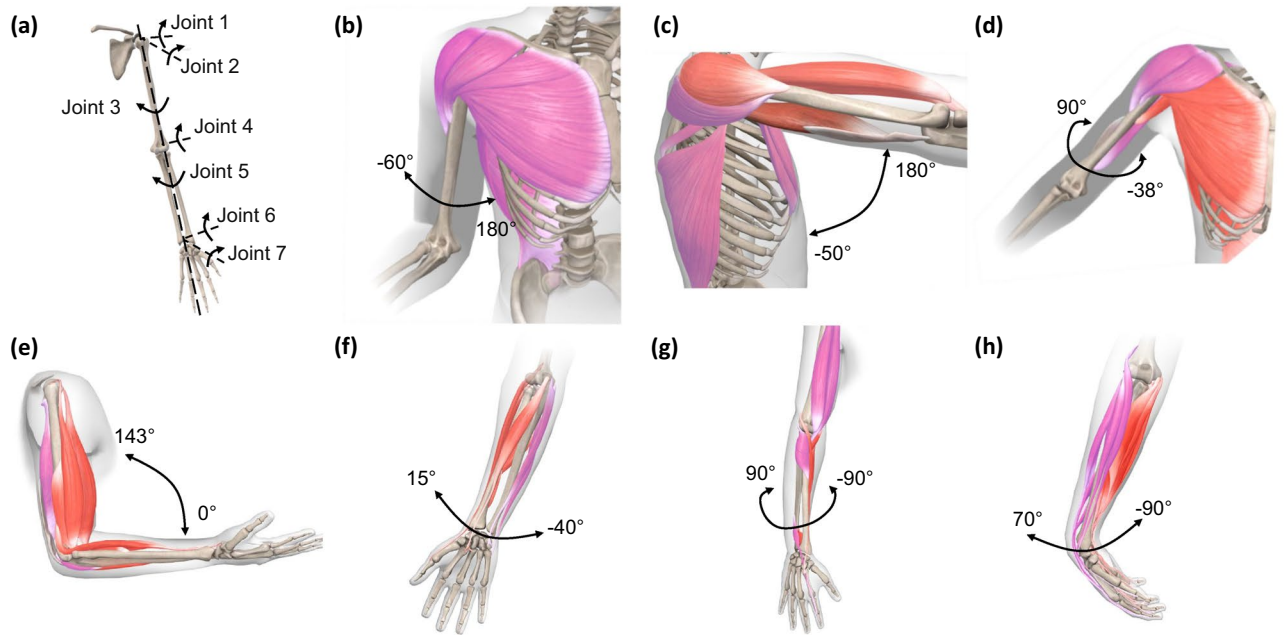


**Fig. 3.** Analysis of the DOF of the human upper limb. (a) seven-DOFs movement. (b) Shoulder lateral rotation and medial rotation. (c) Shoulder flexion and extension. (d) Shoulder abduction and adduction. (e) Elbow flexion. (f) Wrist abduction and adduction. (g) Wrist lateral and medial rotation. (h) Wrist flexion and extension.

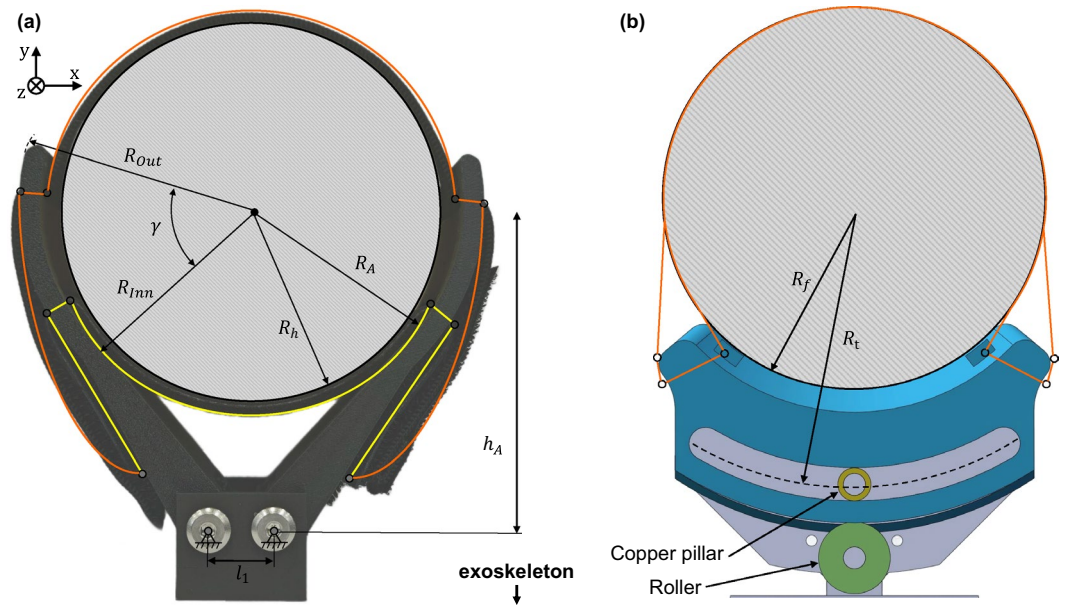


**Fig. 4.** Arm attachment mechanism. (a) Upper arm attachment mechanism. (b) Forearm attachment mechanism.

is as follows: First, a linear relationship between the DC voltage output of the sliding rheostat and the actual arm length is established through experimental calibration. Then, based on the real-time acquired voltage signal, the real-time length of the upper and lower arms is calculated through a mapping function. Subsequently, the exoskeleton URDF model is reconstructed, defining the extension and retraction segments of the upper and lower arms as moving joints and dynamically adjusting the joint spacing of J3-J4 and J4-J5 to match the user's upper limb physical structure. Finally, an updated forward and inverse kinematics algorithm is used to complete real-time end-effector pose calculation and master-slave motion mapping, ultimately improving the synchronization accuracy of master-slave motion and the immersive experience of operation.

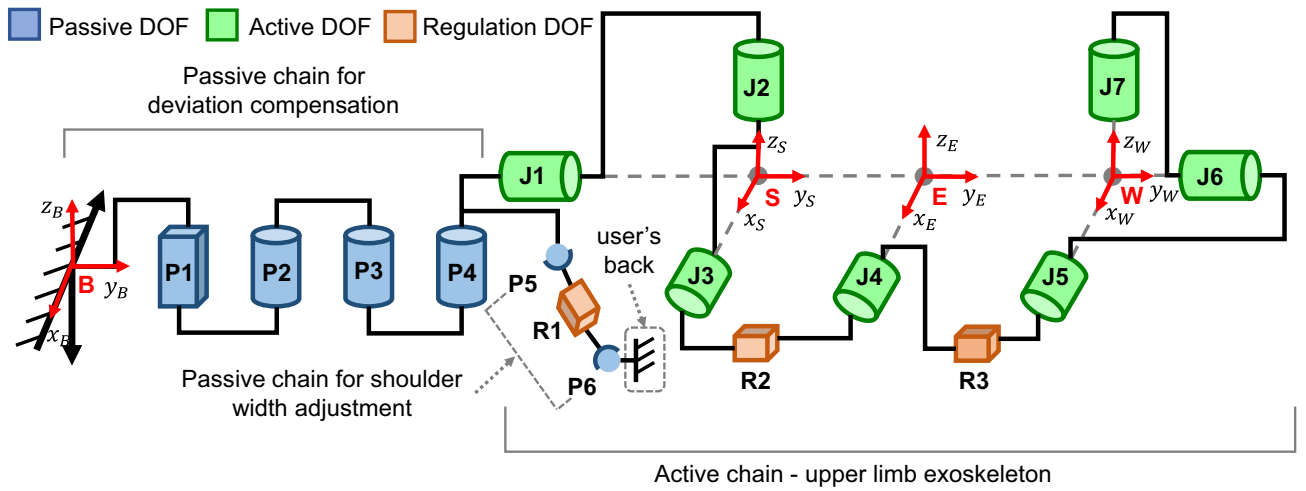


Fig. 5. Schematic diagram of the motion chain.

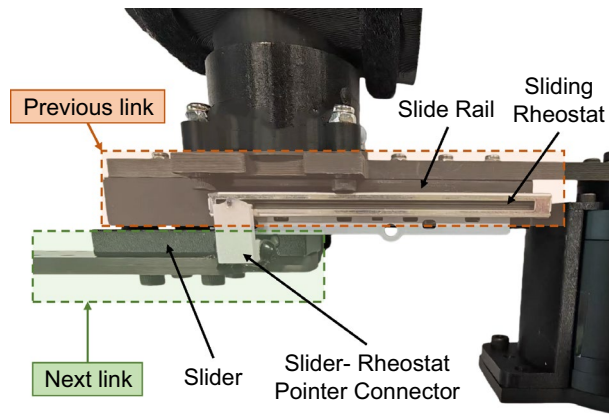


Fig. 6. Arm length parameterization module.

This hybrid kinetic chain architecture improves wearing comfort while ensuring joint range of motion and torque transmission efficiency.

### Control strategy

This paper employs a hybrid control strategy of “master-end position impedance control and slave-end force-based impedance feedback” (Fig. 7): A dynamic model of an upper limb exoskeleton robot is constructed based on the Lagrange equations<sup>33,36</sup>. The joint space dynamic equations of the master-end exoskeleton are as follows:

$$M_h(q_h)\ddot{q}_h + C_h(q_h, \dot{q}_h)\dot{q}_h + G_h(q_h) = \tau_h \tag{1}$$

Where  $M_h(q_h)\ddot{q}_h$  is the inertial force,  $C_h(q_h, \dot{q}_h)\dot{q}_h$  is the Coriolis force,  $G(q) = \frac{\partial P}{\partial q}$  is the gravity load,  $\tau_h$  is the master motor control torque.

$$P = \sum_i m_i g^T p_{ci}(q) \tag{2}$$

$$p_{ci}(q) = p_{oi}(q) + R_{oi}(q)r_{ci} \tag{3}$$

Where  $p_{oi}(q)$  is the position of the origin of the  $i$ th coordinate system in the base coordinate system,  $R_{oi}(q)$  is the rotation matrix of the  $i$ th coordinate system relative to the base coordinate system, and  $r_{ci}$  is the position vector of the centroid in the  $i$ th coordinate system (the local system of the link).

The master end reference joint angle  $q_{d0}$  is measured by the master end sensor, and the master end reference pose  $p_{h,d0}$  is obtained through the analytical solution of the forward kinematics. Based on the D-H parameter method, the master end forward kinematics equations are:

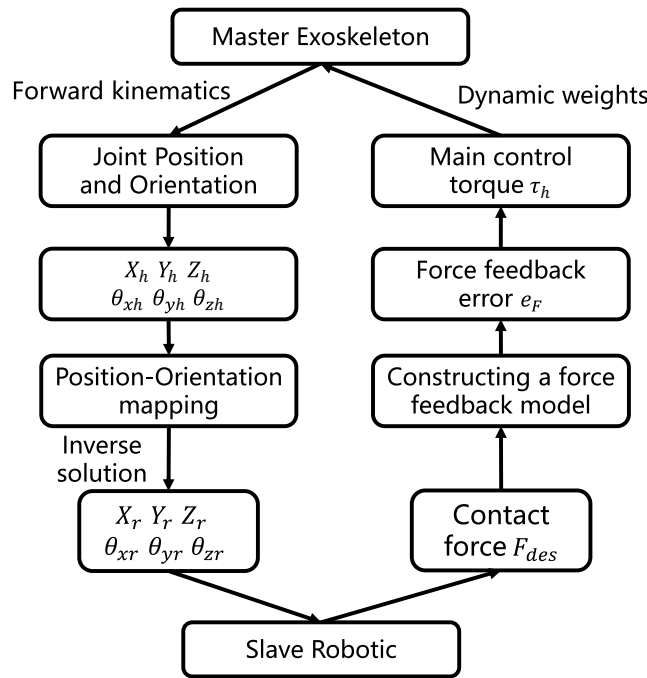


Fig. 7. Workspace-based master-slave mapping flows.

$$p_{h,d0} = T_1(q_{d0,1}) \cdot T_2(q_{d0,2}) \cdot \dots \cdot T_7(q_{d0,7}) \cdot p_7 \tag{4}$$

Where  $T_i(q_{d0,i}) \in \mathbb{R}^{4 \times 4}$  is the D-H transformation matrix of the  $i$ th joint,  $p_7 = [0, 0, 0, 1]^T$  is the homogeneous coordinate of the origin of the terminal coordinate system; the pose vector  $p_{h,d0} = [x_h, y_h, z_h, \phi_h, \theta_h, \psi_h]^T$  (the first 3 dimensions are position, and the last 3 dimensions are roll, pitch, and yaw Euler angles). Then the kinematic equations from the end are:

$$p_{r,d} = [s \cdot x_h, s \cdot y_h, s \cdot z_h, \phi_h, \theta_h, \psi_h]^T \tag{5}$$

Based on the desired end-effector pose  $p_{r,d}$ , the joint angle  $q_r$  is solved using the Newton-Raphson numerical method, where  $s$  is the scaling factor. The contact force  $F_{ext} \in \mathbb{R}^3$  at the end is mapped to the joint torque at the end via the Jacobian matrix at the end, and then mapped to the equivalent torque at the master end via master-slave inertia adaptation<sup>37</sup>:

$$\tau_{ext,r} = J_{p,r}(q_r)^T F_{ext,r} \tag{6}$$

$$F_{ref} = \lambda_f F_{ext,r} \tag{7}$$

Where  $q_r$  is the joint angle after inverse kinematics solution, ensuring that the Jacobian matrix matches the actual joint state of the slave.

The master control aims to track the operator's joint trajectory input while ensuring synchronization of the slave trajectory via end-effector pose mapping. Based on the joint space definition error:

$$e_q = q_d - q_h, \quad \dot{e}_q = \dot{q}_d - \dot{q}_h \tag{8}$$

Where  $q_{d0}$  is the reference joint angle input by the master sensor, and its corresponding end pose has been transmitted to the slave end through Eqs. (4, 5). To achieve accurate trajectory tracking, gravity feedforward compensation and PD-like impedance feedback are introduced:

$$\tau_{pos} = G_h(q_h) + K_p e_q + K_d \dot{e}_q \tag{9}$$

Where  $G_h(q_h)$  is the gravity compensation term,  $K_p e_q$  is the position deviation feedback term, and  $K_d \dot{e}_q$  is the velocity damping term.

The master end desired force feedback model (spring-damped) is constructed based on the actual end-effector pose of the master end:

$$F_{des} = K_f(p_{p,h,act} - p_{p,h,0}) + C_f(\dot{p}_{p,h,act} - \dot{p}_{p,h,0}) \tag{10}$$

Where position  $p_{p,h,*} \in \mathbb{R}^3$ ,  $p_{p,h,act} = f_{FK}(q_h)$  (actual pose of the master end effector), and  $p_{p,h,0}$  is the initial pose. The desired force is mapped to joint force, and the force feedback error is:

$$e_F = F_{ref} - F_{des} \quad (11)$$

Where the force error is converted into a correction amount for the position of the master end, and then mapped into a correction amount for the joint angle:

$$M_a \Delta \ddot{p}_{ff} + C_a \Delta \dot{p}_{ff} + K_a \Delta p_{ff} = e_F \quad (12)$$

$$\Delta q_{ff} = J_{p,h}^\dagger(q_h) \Delta p_{ff} \quad (13)$$

Where  $J_{p,h}^\dagger(q_h)$  is the master-end Jacobian pseudo-inverse, ensuring the dynamic consistency between the position correction and the joint angle correction. The weighting coefficient  $\alpha$  is triggered by the end-contact force, and its value is adapted to the real-time requirements of end-effector pose mapping:

$$\alpha = \begin{cases} 0.85 & \|F_{ref}\| < F_{safe} \\ 0.25 & \|F_{ref}\| \geq F_{safe} \end{cases} \quad (14)$$

Where the adaptive weighting coefficient  $\alpha$  serves as a dynamic arbitration factor between the operator's kinematic intention and the environment's force feedback. As shown in Eq. (14), a threshold-based switching mechanism is designed. When the interaction force is low ( $\|F_{ref}\| < F_{safe}$ ), the system prioritizes high-stiffness trajectory tracking ( $\alpha \approx 0.85$ ) to ensure the exoskeleton faithfully follows the pilot's motion. Conversely, when the force exceeds the safety threshold,  $\alpha$  decreases, rendering the system more compliant to external forces to ensure safety and comfort.

Final expected joint angle at the master end:

$$q_d = \alpha q_{d0} + (1 - \alpha)(q_{d0} + \Delta q_{ff}) \quad (15)$$

At low force, priority is given to ensuring faithful tracking of the operator's input trajectory; at high force, priority is given to force feedback compliance. Substituting Eq. (15) into Eq. (9), the combined force feedback additional torque  $\tau_{ff} = J_{p,h}(q_h)^T F_{ref}$ , the final control torque is:

$$\tau_h = G_h(q_h) + K_p(q_d - q_h) + K_d(\dot{q}_d - \dot{q}_h) + \tau_{ff} \quad (16)$$

To rigorously prove the asymptotic stability of the proposed control scheme, we define the Lyapunov function candidate  $V$  representing the total energy of the closed-loop system:

$$V = \frac{1}{2} \dot{e}_q^T M_h(q_h) \dot{e}_q + \frac{1}{2} e_q^T K_p e_q \quad (17)$$

Where  $M_h(q_h)$  is the inertia matrix which is symmetric and positive definite, and  $K_p$  is a positive definite gain matrix, it follows that  $V > 0$  for all  $(\dot{e}_q, e_q) \neq 0$ , and  $V = 0$  only at the equilibrium point.

Differentiating  $V$  with respect to time yields:

$$\dot{V} = \dot{e}_q^T M_h(q_h) \ddot{e}_q + \frac{1}{2} \dot{e}_q^T \dot{M}_h(q_h) \dot{e}_q + \dot{e}_q^T K_p e_q \quad (18)$$

Substituting the closed-loop dynamics derived from Eq. (16) and the robot dynamics model Eq. (1) (assuming perfect gravity compensation such that  $G_h(q_h)$  is canceled), and utilizing the property that  $M_h(q_h) - 2C_h(q_h, \dot{q}_h)$  is a skew-symmetric matrix (i.e.,  $x^T (M_h - 2C_h)x = 0$ ), the derivative simplifies to:

$$\dot{V} = -\dot{e}_q^T K_d \dot{e}_q \quad (19)$$

Where  $K_d$  is a positive definite damping matrix, we have  $\dot{V} \leq 0$ . This implies that the system is stable in the sense of Lyapunov (the energy is non-increasing). However,  $\dot{V}$  is negative semi-definite because  $\dot{V} = 0$  holds for any state where  $\dot{e}_q = 0$ , regardless of the position error  $e_q$ .

To prove asymptotic stability (i.e.,  $e_q \rightarrow 0$  as  $t \rightarrow \infty$ ), we invoke LaSalle's Invariance Principle. Let  $\Omega$  be the set of all states where  $\dot{V} = 0$ :

$$\Omega = \{(e_q, \dot{e}_q) \mid \dot{V} = -\dot{e}_q^T K_d \dot{e}_q = 0\} \quad (20)$$

In the set  $\Omega$ , since  $K_d$  is positive definite, it must be that  $\dot{e}_q \equiv 0$ . Consequently,  $\ddot{e}_q \equiv 0$ . Substituting  $\dot{e}_q = 0$  and  $\ddot{e}_q = 0$  into the closed-loop error dynamics equation:

$$M_h(q_h) \ddot{e}_q + C_h(q_h, \dot{q}_h) \dot{e}_q + K_d \dot{e}_q + K_p e_q = 0 \quad (21)$$

The terms involving velocity and acceleration vanish, leaving:

$$K_p e_q = 0 \quad (22)$$

Where  $K_p$  is a positive definite matrix and thus invertible, the only solution is  $e_q = 0$ .

Therefore, the largest invariant set contained in  $\Omega$  is the origin  $(e_q, \dot{e}_q) = (0, 0)$ . According to LaSalle's Invariance Principle, the system trajectories asymptotically converge to the origin. This proves that the master end effectively tracks the desired trajectory with global asymptotic stability, ensuring reliable teleoperation performance.

## Experiment

In this section, a Franka Panda robot is utilized to conduct teleoperation verification of the unilateral upper limb exoskeleton. The exoskeleton system runs on a Linux machine equipped with a real-time kernel using the Python programming language. The Franka Panda robot is under real-time control via a dedicated ROS (Robot Operating System) architecture, ensuring reliable and precise motion response. The exoskeleton and the robot are connected through an Ethernet network, enabling the transmission of exoskeleton joint position data at a frequency of 500 Hz to guarantee the synchronization and timeliness of master-slave motion mapping.

### Teleoperation and gravity compensation experiment

As shown in Fig. 8, in the master-slave remote operation experiment, the operator wears an exoskeleton and performs a specified motion task (drawing a figure-eight trajectory in space). During the experiment, a forward kinematics algorithm is used to solve the final pose of the exoskeleton in real time. Subsequently, the final pose of the master end is mapped to the workspace of the slave robotic arm through a master-slave mapping relationship, thus achieving a mirror reproduction of the exoskeleton motion on the Franka Panda robot. The experimental results show that although there is a slight delay (caused by the delay in sending the position data from the PC to the slave robotic arm), the slave robotic arm can still accurately follow the movement of the master exoskeleton.

As shown in Fig. 9, in the gravity compensation experiment, the Lagrange method is used to calculate the torque required for gravity compensation for each joint based on the collected exoskeleton joint angles. The

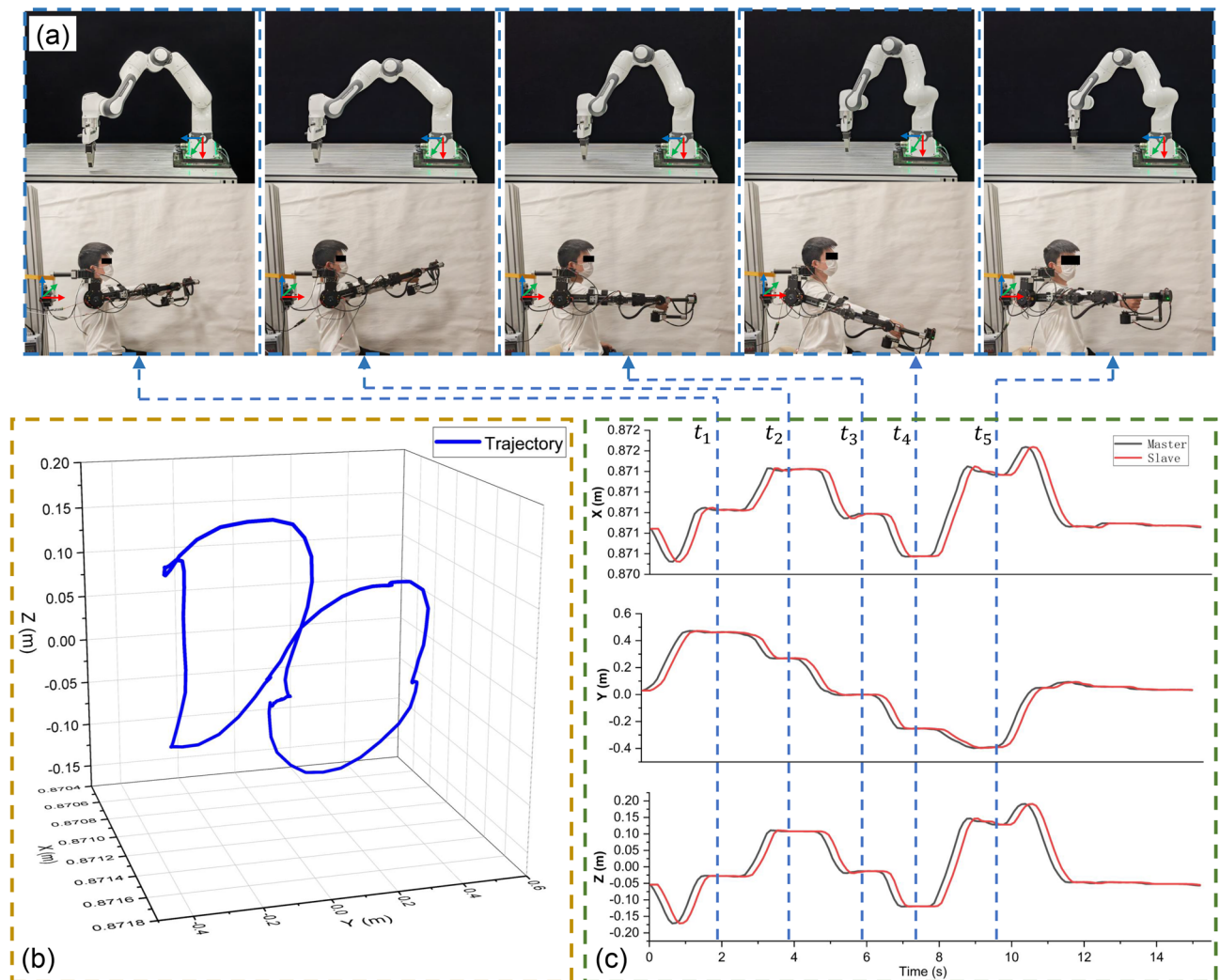


**Fig. 8.** Master-slave teleoperation experiment.

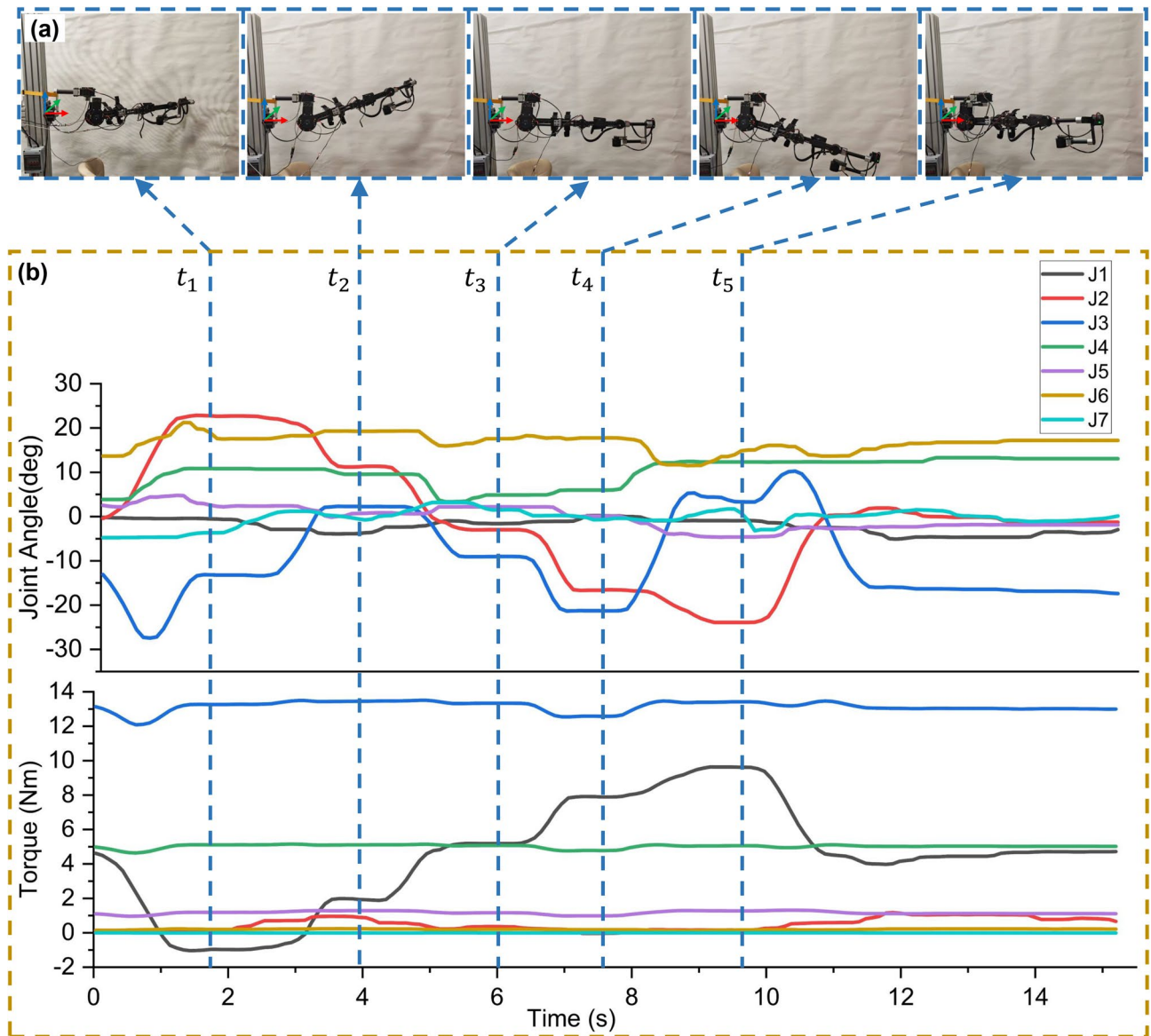


**Fig. 9.** Exoskeleton gravity compensation joint torque.

calculated compensation torque is then distributed to the corresponding joint motors to counteract the gravity load, and the torque output of each joint motor is calculated.

### Ablation study

We performed a 1D normal-contact teleoperation simulation (end-effector constrained by a virtual wall) and report peak contact force, RMS contact force, and free-space RMS tracking error.  $C_0$  uses the baseline master-side position impedance with gravity compensation,  $\tau_{pos} = G_h(q_h) + K_p e_q + K_d \dot{e}_q$ .  $C_1$  adds direct force-reflection torque  $\tau_{ff} = J_{p,h}(q_h)^T F_{ref}$  while keeping  $q_d = q_{d0}$ .  $C_2$  further introduces a virtual compliance block that converts the force error  $e_F$  into a bounded joint offset via the second-order dynamics in Eqs. (12, 13), updating  $q_d = q_{d0} + \Delta q_{ff}$ . This does not replace impedance control with admittance control; it only augments the reference generation by shaping  $e_F$  through a second-order virtual compliant filter to obtain  $\Delta q_{ff}$ .  $C_3$  finally activates force-triggered blending  $q_d = \alpha q_{d0} + (1 - \alpha)(q_{d0} + \Delta q_{ff})$ , where  $\|F_{ref}\|$  switches with  $F_{safe}$ .

The ablation results in Table 3 are obtained under the same 1-DoF normal-contact teleoperation condition: the master is commanded to execute a small-amplitude motion along the selected end-effector normal direction (1D normal axis), while the slave interacts with a rigid virtual wall placed at a fixed normal position  $n_w$  along that direction; all robot models, sampling time, and environment parameters are kept identical across  $C_0$ – $C_3$ . In addition, the reflected-force signal used by the force-related modules is generated from the slave-side contact estimate and mapped to the master side using the same scaling  $F_{ref} = \lambda_f F_{ext,r}$ . Quantitative analysis and ablation experiments revealed three significant trends: First, the free-space motion performance of  $C_1$  is almost

Case	$F_{\text{peak}}(\text{N})$	$F_{\text{rms}}(\text{N})$	$e_{\text{free,rms}}(\text{m})$
$C_0$	23.74	18.39	5.241
$C_1$	23.08	17.94	5.241
$C_2$	17.03	13.72	6.760
$C_3$	7.41	4.27	5.441

**Table 3.** Ablation results in 1-DoF normal-contact teleoperation (rigid wall).

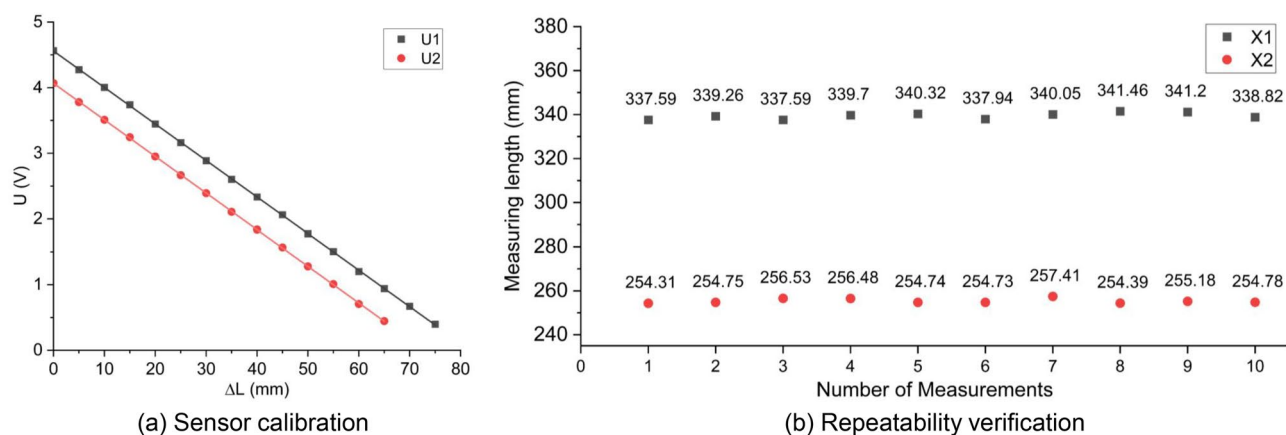


**Fig. 10.** Arm length sensor module evaluation. (a) Sensor calibration. (b) Repeatability verification.

identical to that of  $C_0$ , showing only limited performance improvement during the contact phase. This indicates that, under this experimental setup, relying solely on force-reflecting torque is insufficient to effectively shape the transient characteristics of contact. Second, the activation of the virtual compliance block in  $C_2$  effectively reduces contact impact force, but also leads to a slight decrease in free-space tracking accuracy. This result aligns with the inherent performance trade-offs of the compliance reference shaping strategy. Third, the complete scheme  $C_3$  achieves the optimal balance of the above performance indicators—the introduced force-triggered fusion mechanism significantly suppresses contact force peaks while maintaining free-space tracking accuracy close to the baseline level ( $C_0$ ). Based on these experimental results, it can be inferred that the core performance improvement stems from the proposed adaptive (force-dependent) compliance fusion strategy. Combining this strategy with a torque-based force rendering method can further enhance contact interaction stability without sacrificing free-space motion fidelity.

### Arm length parametric modeling estimation experiment

To achieve real-time measurement of the length of the telescopic boom and arm, this study first calibrated the sliding rheostat installed on the track. In the experiment, the telescopic boom and arm mechanism were fixed on the experimental platform, and the arm length was gradually changed in 5 mm increments within the adjustable range. The corresponding output voltage (V) and actual length (L) of the sliding rheostat were recorded at each position. The collected (V, L) data were linearly fitted using the least squares method to obtain the calibration relationship between length and voltage. The coefficient of determination  $R^2$  and the sum of squared residuals were calculated to evaluate the calibration accuracy. The results show that there is a good linear relationship between the output voltage of the sliding rheostat and the arm length ( $(1 - R^2) < 5 \times 10^{-5}$ ), and the sum of squared residuals  $< 0.002 \text{ mm}^2$ ). As shown in Fig. 10a, the calibration curve is basically linearly distributed.

After completing the sensor calibration, to verify the stability and repeatability of the length sensing in practical application scenarios, this study designed a repeated wearing length consistency experiment. Subjects (upper arm length 339mm, forearm length 256mm) wore the exoskeleton system multiple times following the same wearing procedure, recording the effective upper arm/forearm length  $L_i$  obtained from the output of the sliding rheostat after calibration. The length values obtained from multiple wears were compared with the length  $L_{\text{ref}}$  from the first wear, and the length deviation for each wear ( $\Delta L_i = L_i - L_{\text{ref}}$ ) was calculated, along with its mean, standard deviation, and maximum deviation. The experimental results are shown in Fig. 10b. The arm length measurements were highly consistent across multiple wears, with length deviations all within 2.5 mm. This indicates that the proposed length-sensing scheme has good repeatability and stability under actual wearing conditions, meeting the need for long-term, reliable acquisition of arm length parameters for individualized modeling.

## Conclusion

This study employs a repeatable upper limb exoskeleton engineering approach. The system integrates dynamic stabilization control strategies and gravity compensation control technology, significantly improving operational accuracy and real-time adaptability in complex task scenarios. The system's adjustable arm length parameterization module and upper and lower arm binding attachments enable dynamic alignment of the anatomical axes. Furthermore, this technology can be used to collect upper limb motion data and provide rehabilitation training for hemiplegic patients. With its precise motion capture and force feedback capabilities, the system provides a real-time interactive training platform for neural remodeling. Future research will further develop force feedback functionality, enhancing multimodal feedback fusion and autonomous collaborative control capabilities. On one hand, the system plans to combine electromyography (EMG) signals and eye-tracking technology with existing force-tactile feedback to construct a multidimensional human-computer interaction channel, thereby enhancing the intuitive operating experience in complex environments. On the other hand, the system plans to develop an adaptive mapping algorithm based on reinforcement learning to dynamically optimize master-slave control parameters, thereby addressing the cumulative effects of communication latency and transmission errors.

## Data availability

The datasets generated and analyzed during the current study are included in this article and can be available from the corresponding author upon reasonable request.

Received: 14 October 2025; Accepted: 20 January 2026

Published online: 05 February 2026

## References

1. Wu, W. R., Liu, W. W., Qiao, D. & Jie, D. G. Investigation on the development of deep space exploration. *Sci. China: Tech. Sci. Engl.* **55**, 6 (2012).
2. Zhou, X. et al. A 7 cm-scale spherical underwater robot using piezoelectric double-jet actuator for deep-sea environment. *IEEE/ASME Trans. Mechatron.* **29**, 3277–3288 (2023).
3. Angelopoulos, G., Baras, N. & Dasygenis, M. Secure autonomous cloud brained humanoid robot assisting rescuers in hazardous environments. *Electronics* **10**, 124 (2021).
4. Bogue, R. Robots for space exploration. *Ind. Robot Int. J.* **39**, 323–328 (2012).
5. Nagatani, K. et al. Emergency response to the nuclear accident at the Fukushima Daiichi nuclear power plants using mobile rescue robots. *J. Field Robot.* **30**, 44–63 (2013).
6. Wijayathunga, L., Rassau, A. & Chai, D. Challenges and solutions for autonomous ground robot scene understanding and navigation in unstructured outdoor environments: a review. *Appl. Sci.* **13**, 9877 (2023).
7. Swiecicki, C. C., Elliott, L. R. & Wooldridge, R. Squad-level soldier-robot dynamics: Exploring future concepts involving intelligent autonomous robots. In *Aberdeen Proving Ground (MD): Army Research Laboratory (US) Report* (2015).
8. Nahri, S. N. F., Du, S. & Van Wyk, B. J. A review on haptic bilateral teleoperation systems. *J. Intell. Robot. Syst.* **104**, 13 (2022).
9. Su, Y.-P. et al. Integrating virtual, mixed, and augmented reality into remote robotic applications: a brief review of extended reality-enhanced robotic systems for intuitive telemanipulation and telemanufacturing tasks in hazardous conditions. *Appl. Sci.* **13**, 12129 (2023).
10. Phung, A., Billings, G., Daniele, A. F., Walter, M. R. & Camilli, R. Enhancing scientific exploration of the deep sea through shared autonomy in remote manipulation. *Sci. Robot.* **8**, eadi5227 (2023).
11. Salman, A. E. & Roman, M. R. Augmented reality-assisted gesture-based teleoperated system for robot motion planning. *Ind. Robot* **50**, 765–780 (2023).
12. Smith, R., Cucco, E. & Fairbairn, C. Robotic development for the nuclear environment: challenges and strategy. *Robotics* **9**, 94 (2020).
13. Wang, Z., Reed, I. & Fey, A. M. Toward intuitive teleoperation in surgery: Human-centric evaluation of teleoperation algorithms for robotic needle steering. In *2018 IEEE International Conference on Robotics and Automation (ICRA)* 5799–5806 (IEEE, 2018).
14. Zhang, S. et al. Gait deviation correction method for gait rehabilitation with a lower limb exoskeleton robot. *IEEE Trans. Med. Robot. Bionics* **4**, 754–763 (2022).
15. Chen, Z., Guo, J., Liu, Y., Tian, M. & Wang, X. Design and analysis of exoskeleton devices for rehabilitation of distal radius fracture. *Front. Neurobot.* **18**, 1477232 (2024).
16. Tzvetkova, G. V. Robonaut 2: mission, technologies, perspectives. *J. Theor. Appl. Mech.* **44**, 97 (2014).
17. Dardona, T., Eslamian, S., Reisner, L. A. & Pandya, A. Remote presence: development and usability evaluation of a head-mounted display for camera control on the da vinci surgical system. *Robotics* **8**, 31 (2019).
18. Despinoy, F. et al. Evaluation of contactless human-machine interface for robotic surgical training. *Int. J. Comput. Assist. Radiol. Surg.* **13**, 13–24 (2018).
19. Zhang, Z. & Qian, C. Wearable teleoperation controller with 2-dof robotic arm and haptic feedback for enhanced interaction in virtual reality. *Front. Neurobot.* **17**, 1228587 (2023).
20. Ishiguro, Y. et al. Bilateral humanoid teleoperation system using whole-body exoskeleton cockpit tablis. *IEEE Robot. Autom. Lett.* **5**, 6419–6426 (2020).
21. Ramos, J. & Kim, S. Humanoid dynamic synchronization through whole-body bilateral feedback teleoperation. *IEEE Trans. Rob.* **34**, 953–965 (2018).
22. Palagi, M. et al. Mult: a wearable mechanical upper limbs tracker designed for teleoperation. In *2024 IEEE International Conference on Advanced Intelligent Mechatronics (AIM)* 230–235 (IEEE, 2024).
23. Toedtheide, A., Chen, X., Sadeghian, H., Naceri, A. & Haddadin, S. A force-sensitive exoskeleton for teleoperation: an application in elderly care robotics. In *2023 IEEE International Conference on Robotics and Automation (ICRA)* 12624–12630 (IEEE, 2023).
24. Suarez, A., Gonzalez-Morgado, A. & Ollero, A. Lightweight and compliant bilateral teleoperation system with anthropomorphic arms for aerial and ground service operations. In *2024 IEEE International Conference on Robotics and Automation (ICRA)* 15685–15691 (IEEE, 2024).
25. Zeiaee, A., Zarrin, R. S., Eib, A., Langari, R. & Tafreshi, R. Cleverarm: a lightweight and compact exoskeleton for upper-limb rehabilitation. *IEEE Robot. Autom. Lett.* **7**, 1880–1887 (2021).
26. Pan, J. et al. A self-aligning upper-limb exoskeleton preserving natural shoulder movements: kinematic compatibility analysis. *IEEE Trans. Neural Syst. Rehabil. Eng.* **31**, 4954–4964 (2023).
27. Ning, Y. et al. Design and analysis of a compatible exoskeleton rehabilitation robot system based on upper limb movement mechanism. *Med. Biol. Eng. Comput.* **62**, 883–899 (2024).
28. Easterby, R., Kroemer, K. H. E. & Chaffin, D. B. *Anthropometry and Biomechanics: Theory and Application* (Springer, 1982).

29. Zhang, S. et al. An intelligent rehabilitation assessment method for stroke patients based on lower limb exoskeleton robot. *IEEE Trans. Neural Syst. Rehabil. Eng.* **31**, 3106–3117 (2023).
30. Hogrel, J.-Y. et al. Development of a french isometric strength normative database for adults using quantitative muscle testing. *Arch. Phys. Med. Rehabil.* **88**, 1289–1297 (2007).
31. Rebelo, J., Sednaoui, T., Den Exter, E. B., Krueger, T. & Schiele, A. Bilateral robot teleoperation: a wearable arm exoskeleton featuring an intuitive user interface. *IEEE Robot. Autom. Mag.* **21**, 62–69 (2014).
32. Campioni, L. et al. Preliminary evaluation of a soft wearable robot for shoulder movement assistance. *IEEE Trans. Med. Robot. Bionics* (2025).
33. Pan, J., Wan, J., Wang, Z., Zheng, L. & Jiang, L. Dynamics modeling of spraying robot using lagrangian method with co-simulation analysis. In *2021 IEEE International Conference on Electrical Engineering and Mechatronics Technology (ICEEMT)* 679–683 (IEEE, 2021).
34. Vazquez-Santacruz, J., Portillo-Velez, R., Torres-Figueroa, J., Marin-Urias, L. & Portilla-Flores, E. Towards an integrated design methodology for mechatronic systems. *Res. Eng. Design* **34**, 497–512 (2023).
35. Zimmermann, Y. et al. Human-robot attachment system for exoskeletons: design and performance analysis. *IEEE Trans. Rob.* **39**, 3087–3105 (2023).
36. Siciliano, B., Sciavicco, L., Villani, L. & Oriolo, G. *Robotics: Modelling, Planning and Control* (Springer, 2009).
37. Si, W., Wang, N., Li, Q. & Yang, C. A framework for composite layout skill learning and generalizing through teleoperation. *Front. Neurobot.* **16**, 840240 (2022).
38. Liu, J., He, Y., Yang, J., Cao, W. & Wu, X. Design and analysis of a novel 12-dof self-balancing lower extremity exoskeleton for walking assistance. *Mech. Mach. Theory* **167**, 104519 (2022).
39. Zhang, S. et al. Generation & clinical validation of individualized gait trajectory for stroke patients based on lower limb exoskeleton robot. *IEEE Trans. Autom. Sci. Eng.* (2024).
40. Zheng, L., Wu, Q., Zhu, Y. & Zhang, Q. Design and evaluation of a reconfigurable 7-dof upper limb rehabilitation exoskeleton with gravity compensation. In *2024 IEEE International Conference on Robotics and Automation (ICRA)* 190–196 (IEEE, 2024).
41. Hayami, N. et al. Effect of force feedback during interaction with straight-line movement in a vr space by an upper-limb wearable force feedback device. In *2024 IEEE International Conference on Advanced Intelligent Mechatronics (AIM)* 205–210 (IEEE, 2024).

### Author contributions

P.Zeng and Y.Xu. were responsible for structural design, platform construction, experimental design, and manuscript writing. S.Zheng and S.Zhang were responsible for experimental design and manuscript writing. C.Zhu and R.Huang modified the experimental protocol. Y.Zhang supervised the study and provided technical comments on the experiment. All authors read and approved the final manuscript.

### Funding

This study was partially supported by the Natural Science Foundation of Top Talent of SZTU (GDRC202328) and the National Key R&D Program of China (2024YFB4709900).

### Competing interests

The authors declare no competing interests.

### Additional information

**Correspondence** and requests for materials should be addressed to Y.Z.

**Reprints and permissions information** is available at [www.nature.com/reprints](http://www.nature.com/reprints).

**Publisher's note** Springer Nature remains neutral with regard to jurisdictional claims in published maps and institutional affiliations.

**Open Access** This article is licensed under a Creative Commons Attribution-NonCommercial-NoDerivatives 4.0 International License, which permits any non-commercial use, sharing, distribution and reproduction in any medium or format, as long as you give appropriate credit to the original author(s) and the source, provide a link to the Creative Commons licence, and indicate if you modified the licensed material. You do not have permission under this licence to share adapted material derived from this article or parts of it. The images or other third party material in this article are included in the article's Creative Commons licence, unless indicated otherwise in a credit line to the material. If material is not included in the article's Creative Commons licence and your intended use is not permitted by statutory regulation or exceeds the permitted use, you will need to obtain permission directly from the copyright holder. To view a copy of this licence, visit <http://creativecommons.org/licenses/by-nc-nd/4.0/>.

© The Author(s) 2026